

Impact of Individual Structural Defects in GaAs Solar Cells: A Correlative and In Operando Investigation of Signatures, Structures, and Effects

Qiong Chen, Brandon S. McKeon, Sunny Y. Zhang, Fan Zhang, Changkui Hu, Timothy H. Gfroerer, Mark W. Wanlass, David J. Smith,* and Yong Zhang*

Defects usually degrade device performance. Thus, many techniques and effort are devoted to studying semiconductor defects. However, it is rarely known: i) how individual defects affect device performance; ii) how the impact depends on the device operating conditions; iii) how the impact varies from one defect to another; and iv) how these variations are correlated to the microscopic-scale defect structure. To address these crucial questions, an array of correlative and spatially resolved techniques, including electroluminescence, photoluminescence, Raman, I - V characteristics, and high-resolution electron microscopy, are used to characterize dislocation defects in GaAs solar cells. Significantly, the study is carried out in a series mode and in operando. This approach provides quantitative and definitive correlation between the atomistic structure of defects and their explicit effects on device performance, thus giving unprecedented insight into defect physics.

of structural defects. It is common knowledge that such defects will degrade device performance. There are, in general, two types of defects: point defects (PDs) and extended defects (EDs).^[1–4] The former typically involve one or a few atoms in the following forms: substitutional or interstitial foreign atoms, vacancies, antisites, or their complexes. In contrast, EDs, such as dislocations, can consist of thousands or more atoms that are misplaced from their regular lattice sites. Concerning their impact on device performance, although they differ in detailed electronic structure, an important point is that an ED exhibits much higher density of states than a moderate level of PDs. Therefore, PDs tend to be more impactful for applications

1. Introduction

The ultimate constraint for a solar cell or practically any semiconductor device to reach its theoretical performance limit is the quality of the active material, i.e., the inevitable presence

involving low carrier densities, and EDs are more detrimental for high carrier density applications, because the PDs can be saturated with high carrier density, but the EDs cannot.^[5,6] In fact, the two types of defects often play competing roles in a device. For example, increased carrier density may lead to a larger carrier diffusion length, which in turn makes the adverse effects of EDs more severe, because the ED may sink a large number of carriers within the diffusion length.^[5] Although PDs typically degrade device performance, EDs will not only have the same effect but they are also responsible for the fatal consequence, namely, device failure. Although empirical connections between the degradation of GaAs semiconductor lasers and the formation of so-called dark-line defects were observed decades ago,^[7] it has recently been shown that a simple dislocation defect can indeed mutate into a far more detrimental dark-line defect under high-density optical injection conditions.^[5]

Many characterization techniques are available to probe individual defects for both structure and properties, and are sometimes applied correlatively.^[5,8–18] However, defect studies have typically been conducted in a parallel mode where the wafer is divided into multiple pieces for independent optical and structural characterization, and separate device fabrication and evaluation. Moreover, it is often highly challenging or even impossible to carry out operando characterization in devices at the individual defect level. These limitations explain the general lack of definitive understanding on the impact of individual defects in operating devices. Specifically, it is generally

Dr. Q. Chen, S. Y. Zhang, Dr. F. Zhang, Prof. C. Hu, Prof. Y. Zhang
Electrical and Computer Engineering Department
University of North Carolina at Charlotte
Charlotte, NC 28223, USA
E-mail: yong.zhang@uncc.edu

Dr. B. S. McKeon, Prof. D. J. Smith
Department of Physics
Arizona State University
Tempe, AZ 85287, USA
E-mail: dsmith1@asu.edu

Prof. C. Hu
Department of Physics Science and Technology
Wuhan University of Technology
Wuhan, Hubei 430070, China

Prof. T. H. Gfroerer
Department of Physics
Davidson College
Davidson, NC 28035, USA

Dr. M. W. Wanlass
National Renewable Energy Laboratory
Golden, CO 80401, USA

 The ORCID identification number(s) for the author(s) of this article can be found under <https://doi.org/10.1002/adom.202001487>.

DOI: 10.1002/adom.202001487

unclear: i) how individual defects affect device performance; ii) how the impact depends on the device operation conditions; iii) how the impact varies from one defect to another; and iv) how these variations are correlated to the microscopic-scale defect structure. This type of knowledge would provide more definitive understanding of the defects, in particular for evaluating the need and possible strategies to remove them or mitigate their effects.

There were early attempts at correlative studies of dislocation defects in GaAs ingots using Raman, photoluminescence (PL), electron-beam-induced current (EBIC), and transmission electron microscopy (TEM), but the defects in the ingots exhibited rather different behavior than in epitaxial layers, and the studies were performed with low spatial resolution.^[19,20] Recently, we made a concentrated attempt to correlate PL imaging/chemical etching/scanning electron microscopy (SEM) imaging in CdTe epilayers, and found that etch pits, which are the result of the classical defect study approach of chemical etching, did not always match the dark spots visible in PL imaging.^[12] Although the results of the PL imaging were somewhat better at reflecting the impact of defects in real devices, the PL process still did not reveal how the carriers were generated, injected, or extracted in real electronic or optoelectronic devices, such as transistors, photodetectors, solar cells, and LEDs.

This background of prior work has motivated a more comprehensive investigation, including optical, electrical, and structural characterization, all at the individual defect level.^[21] In this work, we address the issues described above by taking a different approach, i.e., a series mode. Specifically, once a device is fabricated, individual defects on the device are identified. Then, the impact of individual defects is thoroughly analyzed by applying an array of correlative and spatially resolved techniques, including electroluminescence (EL), PL, micro-Raman, and microscale illuminated current–voltage (*I*–*V*) characteristics.^[22] Finally, the atomic-scale defect structure for the same defects are determined using high-resolution TEM. It has been shown previously that defects may be modified or mutate during device operation^[23] or under high density photoexcitation.^[5] This work investigates defects in their as-grown states by limiting the injection current and illumination light density to below the mutation thresholds, so that the native defect structure can be determined by TEM.

2. Results and Discussion

2.1. Optical and Optoelectrical Characterization of Individual Defects

Figure 1 shows a set of EL, PL, and Raman images and spectra obtained from a cluster of dislocation defects in the GaAs device from the region identified as #5-2 (see Figures A1 and A2 in the Supporting Information). EL is first used for a large-area survey to identify potential EDs, which are visible as dark regions in EL images. A few likely structural defects, a group of three dark sites (A, B, and C) with visually different sizes, appear in the EL image **Figure 1a**, which is acquired under 1.25 V forward bias. The comparison between the EL image

and optical image **Figure 1b** excludes the possibility of the observed features in the EL image (marked as red dots in the optical image) being caused by surface blemishes that are visible only in the optical image but not in the EL image. The surface blemishes that are visible in **Figure 1b** are actually amorphous carbon-like parasitic depositions, and do not match the exact locations of the defects (see Figures A3 and A4 in the Supporting Information for more details). PL and Raman measurements are then used to further confirm the identity of the defect located from the EL image, because a dislocation defect tends to exhibit some distinct characteristics in PL and Raman.^[5,24] PL imaging is performed near the triplet, as shown in **Figure 1c**, and the PL spectra between a general site and the largest defect site (#5-2A) are contrasted in **Figure 1d**. These are measured under 5.6×10^4 W cm⁻² excitation density (228 μW). As expected, the PL intensity from the defect site is much lower than from the defect-free spot (1:7.7 ratio). The parasitic surface features actually enhance the PL intensity, which is not of interest to this work. However, surprisingly, the PL peak energy is found to be blueshifted from 868 nm at a general site to 863 nm at the defect site. This finding is not unique to this particular defect but quite common to many defects studied in this and other GaAs samples, although the amount of PL shift varies. One would probably expect a red shift in the PL peak energy at the defect site due to fewer available carriers to fill up the above bandgap states. Although the exact mechanism remains unclear, one possible cause could be the existence of a compressive in-plane strain field near the defect. It was reported that neutron-irradiation induced defects resulted in a bandgap blue shift in GaAs.^[25] **Figure 1e** shows the Raman mapping result near the largest defect, with the Raman spectra from a defect-free site and the defect site shown in **Figure 1f**, measured under the same condition as for the PL mapping. The defect-free site shows two GaAs Raman modes: 296 cm⁻¹ for longitudinal optical (LO) mode and 268.4 cm⁻¹ for transverse optical (TO) mode, whereas the defect Raman reveals a sharper, stronger and redshifted LO mode at ≈ 293 cm⁻¹ and a slightly weaker TO mode at 269.1 cm⁻¹. At first sight, this finding is counter-intuitive, because one would intuitively expect the defect, exhibiting local structure distortion, to yield broader and weaker spectroscopy features. However, it has been concluded that the shift in frequency and change in intensity of the LO Raman mode are due to the difference in carrier density between the defect and defect-free sites,^[24] because the above-bandgap excitation generates an electron plasmon and the measured Raman signal results from the coupled mode of the LO phonon and plasmon (LOPP).^[26] Note that the intrinsic GaAs Raman modes are reported to be 268.1 (TO) and 291.4 (LO) cm⁻¹,^[27] and our own measurements for a GaAs:Cr sample yielded 268.0 and 291.5 cm⁻¹.

2.2. Effect on *I*–*V* Characteristics and Illumination Power Dependence

To quantitatively assess the impact of a defect, we compare the *I*–*V* characteristics of the solar cell illuminated with a focused laser beam directed at a defect site and

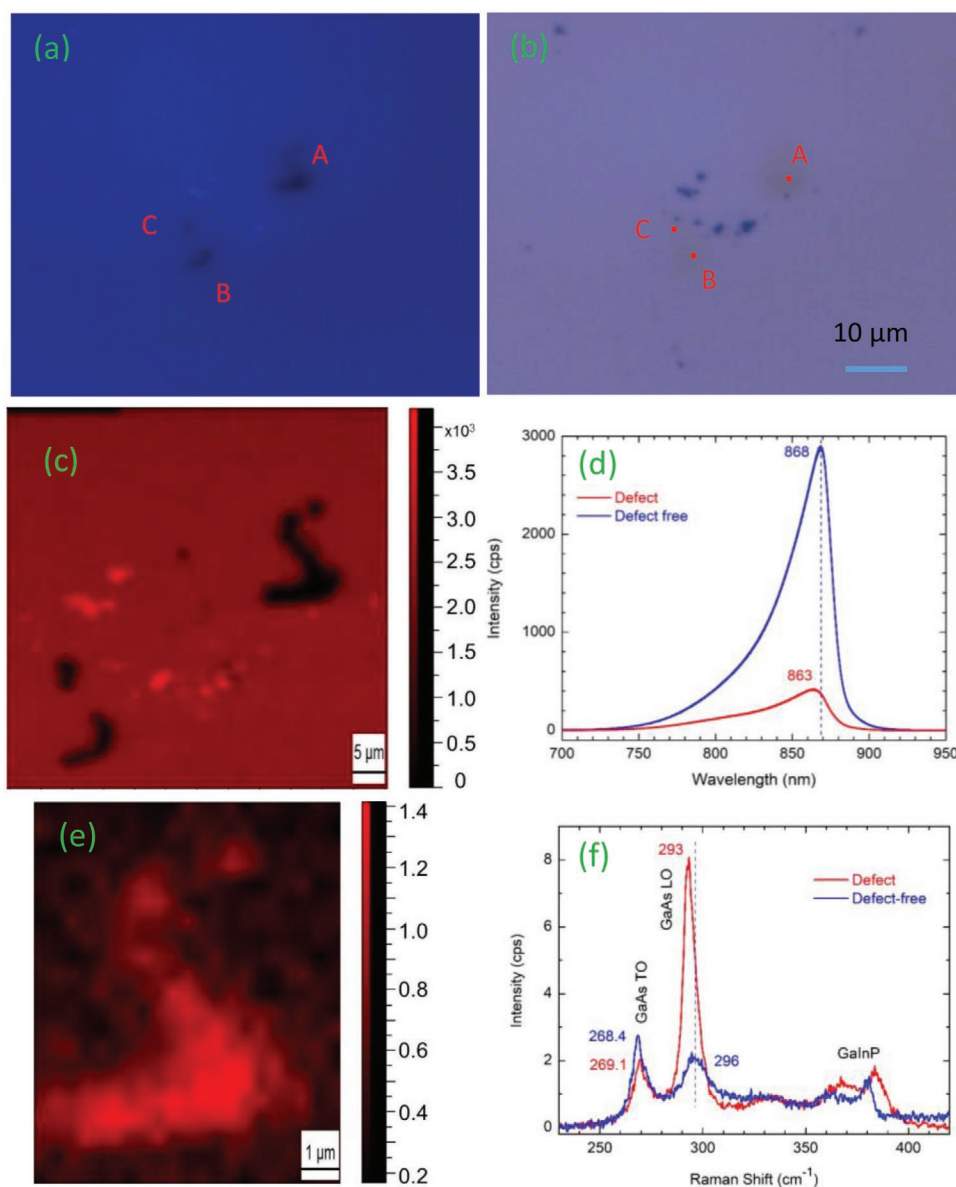


Figure 1. Correlative optical characterization of dislocation defects in a GaAs solar cell. a) EL image using the 50× LWD lens for an area of #5-2 (Figures A1 and A2 in the Supporting Information), showing a cluster of defects; b) optical image of the same area of (a) where the red dots indicate the defect locations; c) PL mapping near the defect cluster using the 100× lens with a beam size approximately shown by the size of the red dot in (b); d) PL spectra from a typical defect-free location and the largest defect (#5-2A); e) Raman mapping near the largest defect (#5-2A); f) Raman spectra from a typical defect-free location and the largest defect in (e).

at a defect-free site, respectively, and varying excitation power. The results for defect #5-2A are summarized in **Figure 2**. First, Figure 2a compares the light and dark I - V curves for cell #5 as a whole. The dark I - V curve indicates a well-behaved diode characteristic. The light I - V curve is obtained using a solar simulator with a power density of 850 W m^{-2} , slightly below 1 sun, giving rise to $I_{sc} = 0.125 \text{ mA}$, $V_{oc} = 893 \text{ mV}$, and $P_{max} = 0.0892 \text{ mW}$ (the maximum point of $P = I V$). Based on the total active device area (the sum of all the strips) of 0.767 mm^2 or $P_L = 0.652 \text{ mW}$, the efficiency of this small cell is $\eta = P_{max}/P_L = 13.7\%$, and the fill factor is $FF = P_{max}/(I_{sc} V_{oc}) = 0.799$. Next, Figure 2b-d depicts

the results obtained using a focused laser under three laser powers (approximately changed over three orders in magnitude), $P_L = 213, 18.5, \text{ and } 1.82 \mu\text{W}$, respectively.

The key performance parameters, I_{sc} , V_{oc} , FF, and η , are obtained from the measured data, and tabulated in **Table 1**. The efficiency calculation for the focused beam is simpler than the macroscopic measurement, since the total illumination power is measured directly by a power meter (no need to calculate the illumination area). The efficiency would be 40.8% higher if reflectance were corrected by multiplying with a factor $1/(1-R)$. All of these key parameters are degraded at the defect site, regardless of the illumination power level,

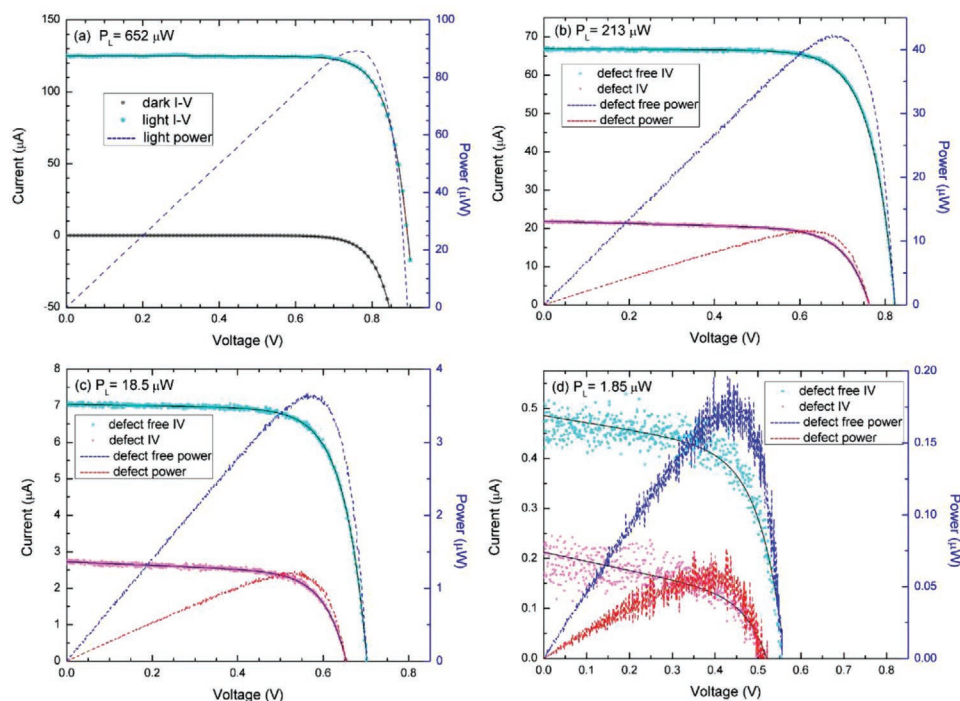


Figure 2. Impact of a defect on solar cell characteristics: left axes for I - V curves (discrete points are experimental data, black solid curves are fitting results), right axes for P - V curves (calculated from experimental data). a) Cell #5 illuminated under approximate one sun. b-d) Comparison between a defect-free site and defect site #5-2A, illuminated with a focused 532 nm laser beam under three laser powers.

but the extent of the degradation depends on the illumination density. Typically, the impact is more significant to I_{sc} than to FF and V_{oc} . For example, I_{sc} is reduced by 67.6%, 61.3%, and 58.5%, respectively, for the three power levels, and the corresponding η reductions are 72.3%, 66.5%, and 68.2%. Because the laser spot size is much larger than the defect core, the I - V characteristic of the “defect site” actually reflects an average effect within the laser spot size which is comparable to the lateral carrier diffusion length in this device. These results provide quantitative assessment of the impact of an individual defect in a solar cell.

It is not straightforward to make direct comparison between the macroscopic and microscopic cell characterization, for example, between Figure 2a,b. The reason is that only a very small area is illuminated in the microscopic measurement, which is approximately equivalent to a circuit with one diode behaving as a solar cell and many parallel diodes under forward

bias, or treating the whole nonilluminated area as the electrode area, thus, resulting in higher dark current.^[22] This condition tends to reduce V_{oc} and FF or distort the light I - V curve, as evident in Table 1, although to much lesser extent in the current device, because it has an overall lower dark current than other thin-film solar cells.^[22] It is interesting that for the two higher laser powers, illuminating a defect-free site with a focused laser beam yields substantially higher efficiency than under uniform illumination of simulated sun light. One reason is that monochromatic irradiance on the long wavelength side of the solar spectrum can yield higher efficiency than the full solar spectrum under the same power.^[28] Another consideration is that the high illumination density can saturate the nonradiative recombination that is rather effective at low illumination density in GaAs,^[6] thus boosting the photocurrent, and leading to overall higher efficiency, compared to distributing the same illumination power uniformly over the whole device area.

Table 1. Summary of characterization results for defect #5-2A. The first row is for the macroscopic results of #5 as a whole, measured under approximate 1 sun ($\approx 850 \text{ W m}^{-2}$). The remaining rows are microscopic results measured using a diffraction-limit laser beam of 532 nm. The error bars are given as superscripts for the key parameters. The efficiency values in parentheses have been corrected for the reflectance loss.

P_L [μW]	Site	I_{sc} [μA]	V_{oc} [mV]	FF	η [%]	I_0 [pA]	n	R_{sh} [$\text{M}\Omega$]	R_s [$10^{-3} \Omega$]
652	whole cell	$125^{\pm 0.2}$	$893^{\pm 0.1}$	$0.799^{\pm 0.003}$	$13.7^{\pm 0.1}$ (≈ 19.3)	0.778	1.83	4.75	0.90
213	defect-free	$66.9^{\pm 0.3}$	$822^{\pm 0.5}$	$0.766^{\pm 0.007}$	$19.8^{\pm 0.1}$ (27.9)	17.9	2.11	1.57	3.93
	defect	$21.7^{\pm 0.3}$	$762^{\pm 0.5}$	$0.708^{\pm 0.02}$	$5.49^{\pm 0.1}$ (7.73)	20.1	2.15	0.356	3.82
18.5	defect-free	$7.03^{\pm 0.02}$	$701^{\pm 0.5}$	$0.728^{\pm 0.011}$	$19.4^{\pm 0.2}$ (27.3)	11.1	2.04	4.76	1.71
	defect	$2.72^{\pm 0.02}$	$655^{\pm 0.5}$	$0.674^{\pm 0.022}$	$6.49^{\pm 0.16}$ (9.14)	7.88	2.01	2.08	6.43
1.82	defect-free	$0.468^{\pm 0.04}$	$556^{\pm 2}$	$0.653^{\pm 0.067}$	$9.34^{\pm 0.55}$ (13.2)	21.0	2.21	7.09	4.82
	defect	$0.194^{\pm 0.04}$	$510^{\pm 8}$	$0.546^{\pm 0.146}$	$2.97^{\pm 0.44}$ (4.18)	5.11	2.05	5.08	2.83

More insight into the effects of individual defects can be obtained from analyzing the measured I - V curves by fitting with a standard I - V characteristic model for a solar cell^[29,30]

$$I = I_L - I_0 \left(e^{\frac{q(V+IR_s)}{nkT}} - 1 \right) - \frac{V + IR_s}{R_{sh}} \quad (1)$$

where I_L is the photogenerated current, I_0 is the dark reverse saturation current, V is the photovoltage generated by the solar cell, n is the diode ideality factor ($n = 1$ for an ideal diode), R_{sh} is the shunt resistance (ideally infinity), and R_s is the series resistance (ideally zero). Additionally, q is the electron charge, k is the Boltzmann constant, and T is the temperature in Kelvin.

Strictly speaking, because of the nonuniform illumination, Equation (1) does not apply for the case of focused illumination. However, since the I - V curves under focused illumination appear similar to a typical well-behaved solar cell, they can be effectively fitted using Equation (1). The fitting curves are plotted in Figure 2b–d, and show excellent agreement with the measured data. The effective n , R_{sh} and R_s values are obtained from the fitting, and are tabulated in Table 1. The values of R_s are very small (in the order of $10^{-3} \Omega$) for all cases. Quantitative comparison of I_0 and n between either uniform and focused illumination or defect-free and defect site is not straightforward, other than noting that I_0 is significantly larger for focused illumination, as expected. A more important finding between the defect-free and defect sites is that the latter consistently yields lower shunt resistance under the same illumination power, and more so for higher illumination power. This trend can be explained as follows: first, the dislocation defect provides a shunt to the photogenerated carriers; second, the effect is more significant for high excitation density, because the effect of the point defects is saturated, and the dislocation defect becomes more prevalent. This understanding is consistent with our previous observations on the dependence of the effective impact area of a dislocation defect in quenching PL with varying excitation density.^[5,31]

Despite the measurement being conducted at one wavelength, the results can provide useful insight to the impact of the defect if the device is illuminated by the full solar spectrum. Because a defect usually captures the photogenerated carriers after they relax to the band edge, to examine the impact of the defect, as an approximation, one can assume the same reduction in quantum efficiency, which can be calculated by $(I_{sc}/e)/(P/h\nu)$, for all wavelengths above the bandgap. In a special case, if the whole solar spectrum illumination has the same number of above-bandgap photons as the single wavelength illumination, the effects are expected to be similar. Alternatively, one unit of power at 532 nm can yield the same number of the above-bandgap photons that 1.466 unit of power of solar spectrum (approximated by that of 6000 K blackbody) can provide.

2.3. Comparison of Different Defects

Different defects have different structure so their impact will be different. Thus, we compare several dislocation defects measured under the same conditions in terms of their PL, Raman, and I - V characteristics. **Figure 3** compare the three

neighboring defects, #5-2A, #5-2B, and #5-2C, as shown in Figure 2, and another defect, #5-3A, from area #5-3 (see Figures A1 and A2 in the Supporting Information). Figure 3a,b are respectively the PL and Raman mapping results near defects #5-2B&C, and Figure 3c,d are the same results for defect #5-3A. They are qualitatively similar to the corresponding results for #5-2A, Figure 2c,e. Figure 3e,f compares, respectively, the PL and Raman spectra of the four defects and the defect-free site. Attempt was made to select the location within each defect that yielded the strongest LO Raman mode intensity and also approximately the lowest PL intensity. Evidently, as shown in Figure 3e, PL peak positions of the GaAs peak are rather different for different defects, but all are blueshifted from the defect-free value: 858–867 nm or $\delta E = 17$ –2 meV relative to 868 nm of the defect-free site. There is also some variation in the vicinity of each defect (not shown). Within #5-2A, #5-2B, and #5-2C, the amount of reduction in PL intensity seems to correlate with the visual size of the defect with the largest defect #5-2A, shown in Figure 1c, also exhibiting the most intensity reduction. Figure 3f compares the Raman spectra of the four defects. There is qualitatively an anticorrelation between the PL intensity and LO mode Raman intensity among the four defects, which can be qualitatively explained by the opposite dependences on the carrier density for PL and Raman.^[24]

As shown in Figure 3f, the TO modes at the defect sites are slightly blueshifted (0.3 – 0.6 cm^{-1}) relative to the defect-free site. Since the TO mode is not sensitive to the carrier density, the shift can be explained as the existence of compressive strain in the defective region, which is consistent with the blueshifts observed in PL, as shown in Figure 3e. Although a simple dislocation defect may induce local strain, the effects are expected to be relatively weak: a less than 0.1 cm^{-1} shift of the LO mode frequency.^[32] Dislocations were reported to relax the TO selection rule (forbidden for (001) backscattering),^[19,20] but this effect is minimal for the dislocation defects studied here, as evident in Figure 3e. These discrepancies are discussed later.

Figure 3g,h depicts their I - V characteristics under two illumination powers (2.1 and 225 μW) for comparison between the four defects. The results for #5-2A are similar to those shown in Figure 2, although there are slight differences because the results of Figures 2 and 3 were from two measurements where the illuminated positions were not exactly the same. The severity of the impact is found in the order of A, B, and C, with A being the strongest for the three defects in area #5-2, whereas the impact for #5-2A and #5-3A are comparable.

It is of interest to compare the effects of the defect on the GaInP window layer. As shown in Figure 3e, #5-2A exhibits the lowest intensity in the GaInP PL, which suggests that if a defect has more negative impact on the absorber layer, it also tends to impact the window layer more. However, to the contrary, although #5-3A also causes a major intensity reduction of the GaAs PL (the second most reduced among the four defects), the intensity of the GaInP PL at #5-3A is not reduced but somewhat stronger. The contrast between #5-2A and #5-3A is actually related to the difference in defect structure, which is discussed later. We also notice that the GaP-like GaInP LO modes near $\approx 380 \text{ cm}^{-1}$ ^[33] are blueshifted to different extent at the defect sites, which seems to suggest the window layer at the defect site is under tensile strain caused by the defect.

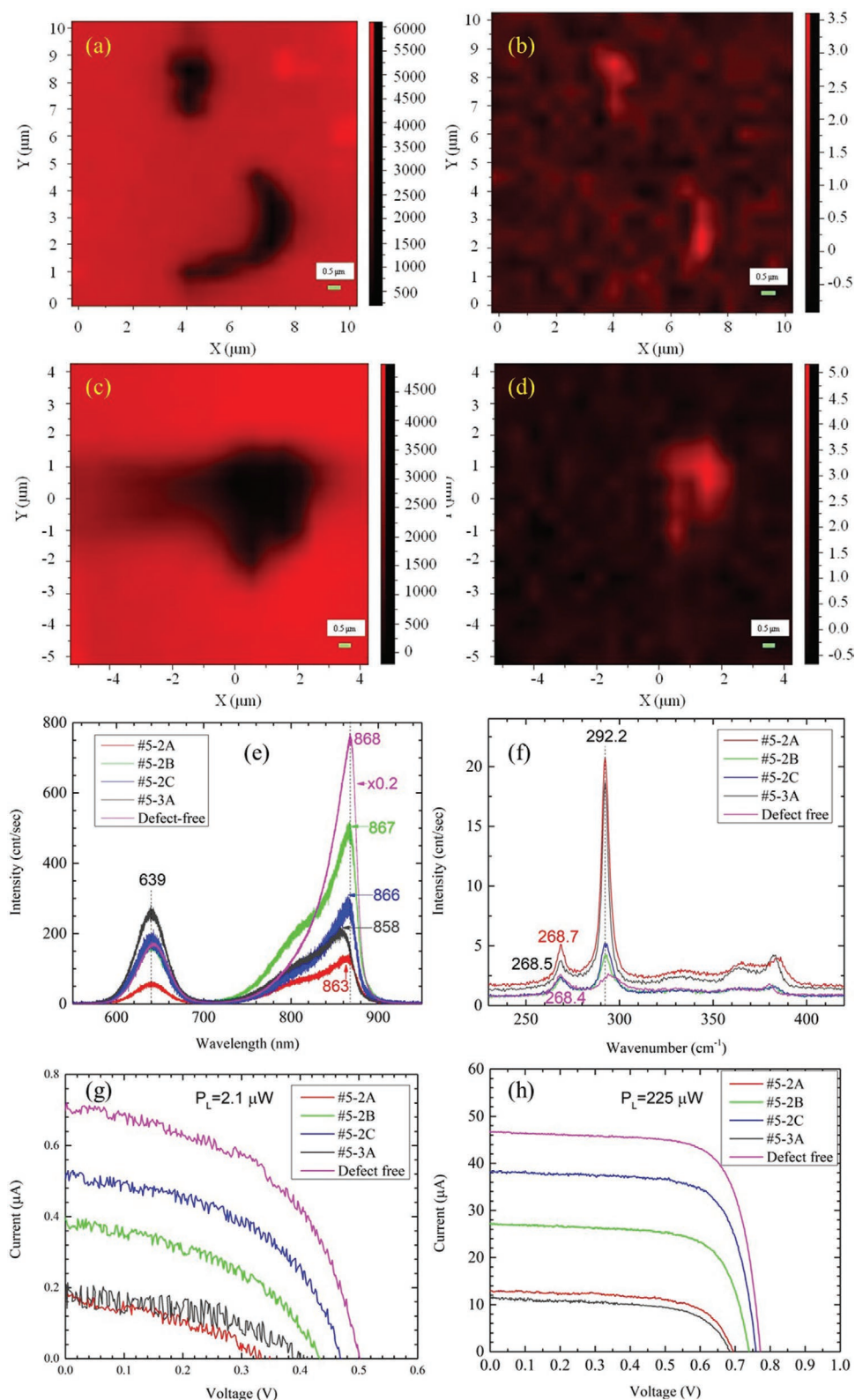


Figure 3. Comparison of different defects. a,b) PL and Raman mapping of defect #5-2B and #5-2C. c,d) The same for defect #5-3A. e,f) PL and Raman spectra of defect #5-2A-C and #5-3A, and a defect free site. g,h) The same in I - V characteristic under two illumination powers.

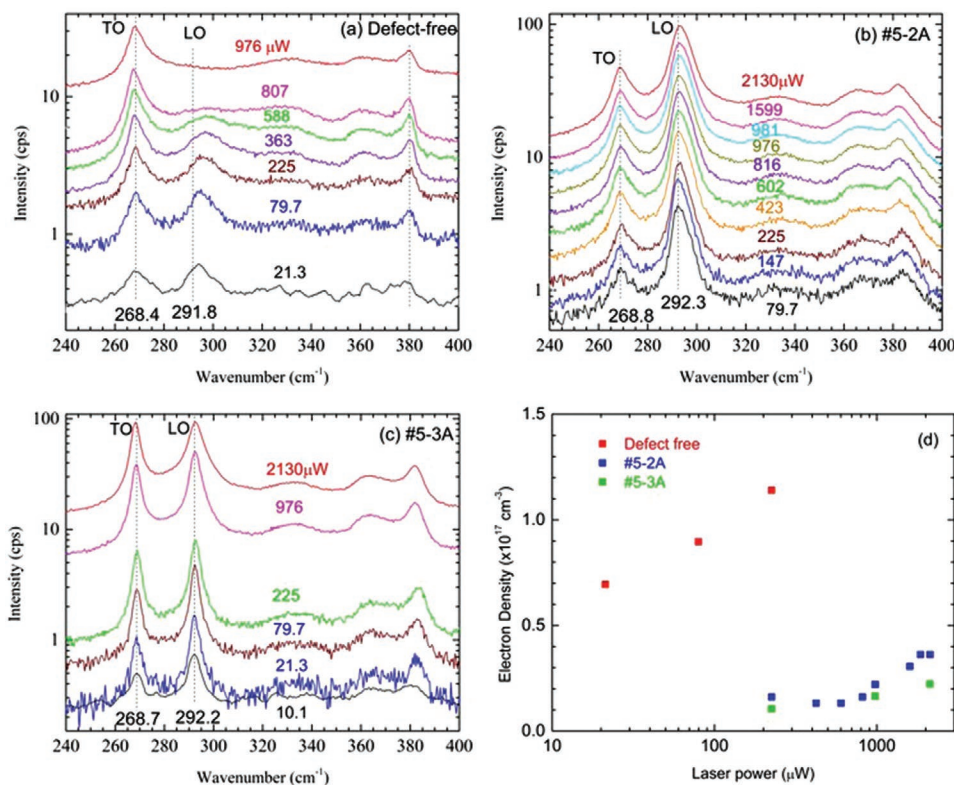


Figure 4. Comparison of Raman spectra and carrier densities with varying excitation laser power for defect-free and defect sites. a–c) Raman spectra for the defect-free site, defect #5-2A, and #5-3A, respectively. Vertical dashed lines indicated the TO and LO frequencies at the low-density limit. d) Carrier densities at different excitation powers.

We can further determine and compare the carrier densities at different defect sites and the defect-free site by using the LOPP coupled mode method.^[24] **Figure 4** shows Raman spectra measured at different excitation powers from two defect sites, #5-2A and #5-3A, and one defect-free site, respectively, in **Figure 4a–c**. **Figure 4d** plots the extracted carrier (electron) densities of the three sites. The TO and LO frequencies vary slightly between the defect-free site and the defect site, due to strain at the defect site. Even for the defect-free site, they are also slightly different from the literature values,^[27] possibly due to residual strain in the epilayer. The coupled mode frequency depends on the TO and LO frequencies at zero carrier density. We take (TO) 268.4 and (LO) 291.8 cm^{-1} for defect-free site, 268.8 and 292.3 cm^{-1} for defect #5-2A, and 268.7 and 292.2 cm^{-1} for defect #5-3A, by taking into account the $\delta\omega_{\text{LO}} \approx 1.2 \delta\omega_{\text{TO}}$ for the bi-axial strain induced shifts,^[34] We use the LOPP mode peak position to determine the carrier density,^[26] instead of a more accurate method—fitting the whole Raman peak line-shape,^[27] because the interference of the GaInP Raman signal makes it difficult to unambiguously isolate the GaAs LOPP mode in the spectra under high excitation power, see **Figure 4a**. There is slight heating at the high laser power points, causing a small redshift in Raman frequency. The shift in the TO mode is used to correct for the shift in the LO mode. Evidently, as shown in **Figure 4a,d**, there is a background electron density at the defect-free site under the lowest excitation density, about $7 \times 10^{16} \text{ cm}^{-3}$. This value can be explained as the background

electron density of the emitter layer that was doped to a much higher level, but the carriers are partially depleted by the surface and trapped by PDs. However, at the defect sites, the electrons in the emitter layer are mostly depleted by the dislocation defects, to the level that cannot be determined reliably using this method (the variation between 200 and 600 μW region reflects the uncertainty); and even under high excitation the electron densities remain much lower than the defect-free site, as shown in **Figure 4b–d**.

2.4. Structural Characterization of Individual Defects

After optical and optoelectronic characterization of individual defects was completed, the defect locations were carefully noted, typically with respect to nearby recognizable surface features, so that they could be located again using the SEM in the dual-beam FIB system. Multiple defects were investigated. Here we highlight results for two of them: #5-2A and #5-3A.

Figure 5 shows low magnification TEM and atomically resolved STEM images for #5-2A. The PL image in **Figure 1c** indicated that this defect was laterally more extended than most of the others. A thin slice of the specimen was extracted from the device at the approximate location indicated on the PL image included with **Figure 5a**. **Figure 5a** reveals that this defect cluster is confined mostly to the GaAs emitter layer and penetrates only a short distance downwards into the GaAs base

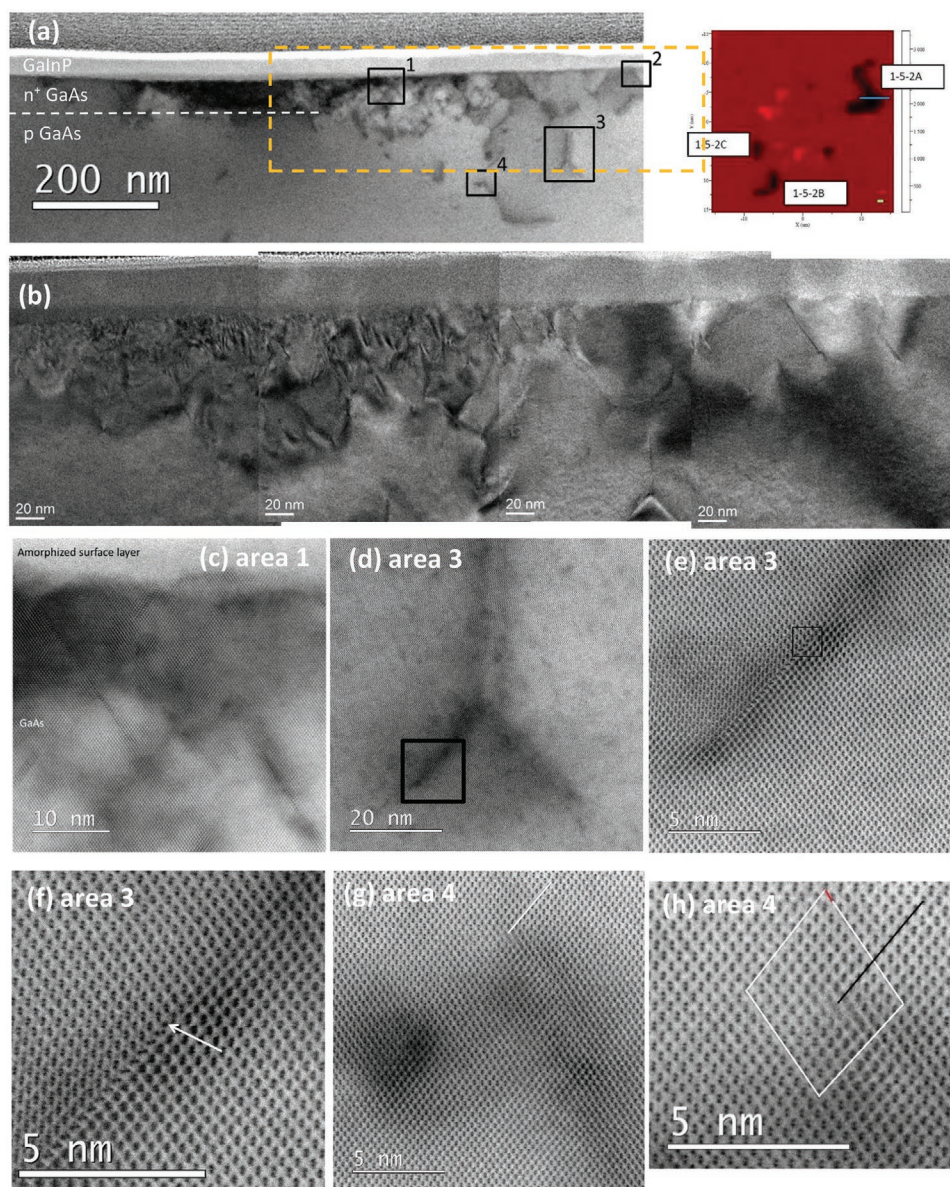


Figure 5. TEM images of defect #5-2A. a) Low magnification image of defective region; b) Enlargement taken from the area indicated by the yellow box in (a). c–h) High-resolution images of areas indicated in (a): c) from area 1; d–f) from area 3 with different magnification, where in e) the end of the stacking fault marked by a black square ends in a 30° partial dislocation while the other end terminates in a 90° partial dislocation, and in f) enlarged view of the area marked by the black square has a single atomic column of arsenic atoms at the core of the 30° partial dislocation (marked by white arrow). g,h) From area 4: g) 60° dislocation near top of the image. The extra half-plane of paired columns is indicated with a white line. h) Enlarged view of 60° dislocation in (g). Burgers circuit is shown in white with the resulting Burgers vector shown in red; the extra half-plane is marked in black.

(absorber) layer, but extends by more than one μm laterally. However, the GaInP window layer in this region seems to be free of defects. An enlargement is shown in Figure 5b. This is clearly a massive defect combining many separate structures. Some of these areas have been examined more closely. High-resolution images were taken from the four areas indicated in Figure 5a. Areas 1 and 2 include the GaInP/GaAs interface. The structures of the area 1 and 2 are similar, as shown in Figure 5c for area 1, which indicates that the top region of the device (the GaAs contact layer and part of the GaInP window layer) is amorphized. The area 3, shown enlarged in Figure 5d–f, has

a stacking fault, where the end of the stacking fault marked by a black square in Figure 5e ends in a 30° partial dislocation while the other end terminates in a 90° partial dislocation. An enlarged view of this area is given in Figure 5f. According to analysis of a HAADF STEM image of the same area (not shown here), the single atomic column at the core of the 30° partial dislocation (marked by the white arrow) is composed of arsenic. Area 4, as shown in Figure 5g,h, exhibits a 60° dislocation near the top of the image, and the extra half-plane of paired columns is indicated by the white line in Figure 5g. An enlarged view of this dislocation is shown in Figure 5h: the Burgers circuit

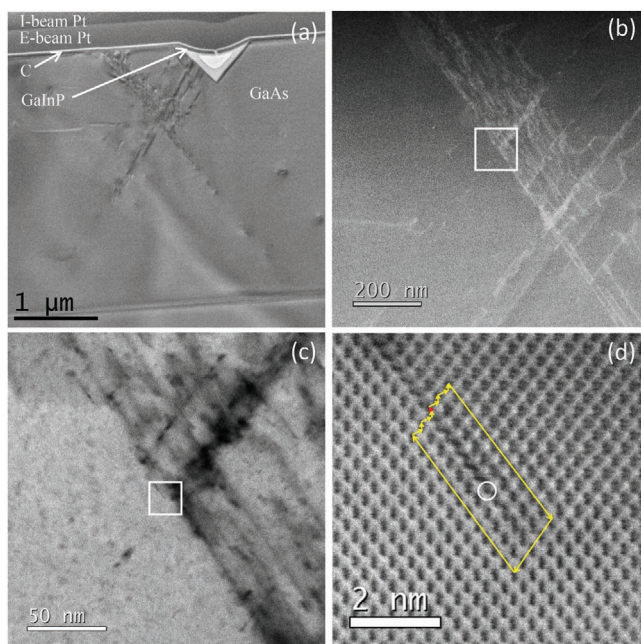


Figure 6. TEM images of defect #5-3A. a) Low magnification image of defective region (note the triangular-shaped pit beneath sample surface adjacent to the defect cluster); b) HAADF image, and c) LABF image, showing major intersection of stacking defects and dislocations. d) Aberration-corrected LABF STEM image of an intrinsic stacking fault terminated by a 30° partial dislocation as identified by the Burgers' circuit shown in yellow. Single As atomic column (circled) at the defect core.

is shown in white, with the resulting Burgers vector shown in red. The extra half-plane of atoms is marked with the black line.

Figure 6 shows the results of microscopic characterization of defect #5-3A, which is structure-wise distinctly different from #5-2A. In the optical image of the device (Figure A6, Supporting Information), there is a white spot right next to the EL dark spot. The low-resolution TEM image in Figure 6a reveals that the white spot corresponds to a pit-like feature in GaAs near the device surface which is covered over by the GaInP window layer, while the dark spot in the EL map is caused by the defect cluster adjacent to the pit. This defect cluster extends mostly along $\{111\}$ -type directions from the surface of the solar cell down into the absorber material for at least $2\ \mu\text{m}$, but not all the way through to the back-surface confinement layer. However, it is far less extended laterally compared to #5-2A. It includes many structural defects, which are mostly concentrated in the top $1\text{-}\mu\text{m}$ of the absorber layer. Figure 6b is a HAADF image showing a major intersection of defect clusters and Figure 6c is a corresponding LABF image taken at higher magnification. Figure 6d is a LABF STEM image of the area in white square in Figure 6c, showing a single 30° partial dislocation that terminates an intrinsic stacking fault. The dislocation type is identified in Figure 6d by drawing a Burgers circuit around the defect, as shown by the yellow arrows. The resulting projected Burgers vector is indicated by the red arrow. The extended stacking fault is terminated by a single, unpaired atomic column indicated by the white circle in the figure, which is identified as corresponding to As.

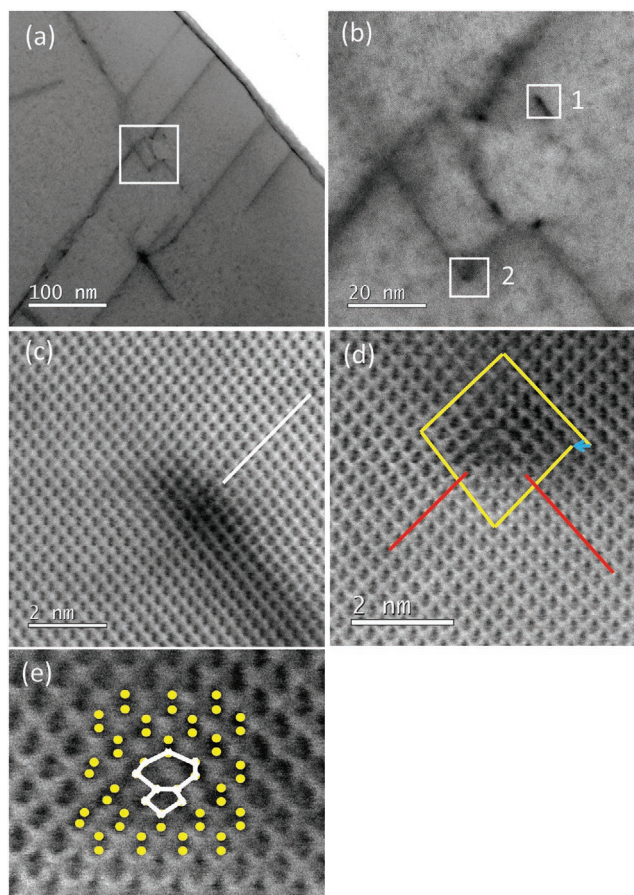


Figure 7. TEM images of defects in the vicinity of the surface pit adjacent to defect #5-3A. a) Low-magnification LABF image showing defects along the edge of surface pit visible in Figure 6a; b) enlargement from the boxed region in (a); c) aberration-corrected LABF image from boxed region 1 in (b) showing 60° perfect dislocation; d) aberration-corrected LABF image from boxed region 2 in (b) showing Lomer edge dislocation; e) enlarged view of Lomer dislocation shown in (d) with overlay showing location of individual atomic columns. Dislocation core shows classic 5- and 7-member ring structure.

The region near the surface pit visible in Figure 6a was also examined for defect structures, with some of the results shown in **Figure 7**. Figure 7a is a low-magnification LABF image from the edge of the pit, with Figure 7b giving an enlarged view of the white square in Figure 7a. Two locations in Figure 7b were examined more closely at higher magnification. Figure 7c is a LABF-STEM image of location 1 containing a perfect 60° dislocation, but no associated stacking fault. An additional plane of atomic columns, often termed a half-plane, is marked by the white line. Figure 7d is a LABF-STEM image of location 2 where lines of strain contrast intersect resulting in a Lomer dislocation. The Burgers circuit drawn to identify the defect is shown with yellow arrows, and the resulting Burgers vector is indicated by the light blue arrow. Lomer dislocations are commonly associated with two extra atomic planes, indicated in the figure with red lines, which terminate at the dislocation core. Figure 7e is an enlarged view of the dislocation core with the approximate locations of individual atomic columns marked by yellow dots. The

white lines in the image show the 5- and 7-member rings that are commonly associated with Lomer dislocations.^[35]

Overall, these observations reveal that those defects showing major impact on optoelectronic performance (e.g., in terms of reduction in PL intensity and photocurrent) were most often associated with a cluster of EDs rather than a single ED, as had been previously assumed.^[5] In addition to the two EDs discussed in detail above, further examined defects supported this conclusion (see, for instance, another example shown in Figure A7 in the Supporting Information). These findings explain why the phonon frequency shift observed at the defective region, presumably associated with the defect induced strain, tends to be larger than that expected for a simple dislocation.^[32] Although we did not observe significant change of the TO mode intensity at the defect site, as one would have expected resulting from relaxation in selection rule due to defect induced disordering,^[19,20] we do observe a strongly enhanced TO Raman mode at the location of the pit, as shown in Figure 6a, which has {111} like surfaces for which TO Raman scattering is allowed.

Each defect cluster was unique, yet sharing common characteristics. Visual comparison of the different defect clusters showed that every cluster was dominated by a collection of extended {111}-type stacking faults, mostly located near the top of the device in the GaAs emitter and absorber layers. These defects typically initiate within the absorber layer at around 0.5–1.5 μm from the lower GaAs/GaInP interface, and pass through the GaAs emitter and the GaInP window layer, which is in contrast to the common belief that such dislocation defects originate from the substrate that happens to have comparable defect density. However, one defect cluster (#5-2A), with relatively short stacking faults, remained mostly confined to the GaAs emitter layer, leaving the GaInP window layer free of defects, and only extended down into the GaAs absorber layer over a short distance ($\approx 0.25 \mu\text{m}$). It might seem counter intuitive that GaInP PL signal is weaker from the nondefective GaInP site (#5-2A) than the defective GaInP site (#5-3A), as shown in Figure 3e. The reason could be that the carriers in the former case are mostly captured by the underneath defect in the GaAs layers, whereas in the latter case the carriers are localized to the GaInP layer itself.

Individual defects in each cluster were comprised primarily of 30° and 90° partial dislocations associated with intrinsic stacking faults, and it was possible in some cases, to identify the chemical species of individual atomic columns at the core of 30° partial dislocations. Although partial dislocations were associated with each defect cluster with long stacking faults, 60° perfect dislocations and Lomer dislocations were also identified in the comparatively shallow defect cluster adjacent to the surface pit. Lomer dislocations with localized strain contrast were revealed at locations where two {111}-type stacking faults intersected. The other defect clusters exhibited far fewer of these intersections and no Lomer dislocations were present in those clusters.

We note that the lateral extensions of the defects identified in these epitaxially grown solar cells are much smaller than the dislocation defects observed in GaAs ingots, which are intended to be used as substrates, with lateral sizes in the order of 100 μm .^[19,20] Moreover, dislocation defects originated from the substrate, e.g., in SiC,^[18] are often found to be much larger in lateral size.

3. Concluding Remarks

This study provides unique insights for both fundamental understanding of defect physics and practical knowledge of the adverse effects of defects at the single defect level. For GaAs solar cells investigated in this work, it has been shown that the most detrimental extended defects identified optically are usually not in the form of a simple dislocation. Instead, each consists of multiple adjacent dislocations, and furthermore each dislocation defect is a complex array of different types of dislocations. In contrast to the common belief that the dislocations are generated from the substrate, the studied defects are all located in the middle of the epitaxial layer with total thickness of a few micrometers. In fact, the defects found in the epilayer are rather different from those in substrates reported previously. The impact of the dislocation defect on the solar cell performance parameters tends to be more significant at higher illumination density, because of the competing roles of point and extended defects. In addition to reduction in photocurrent and open-circuit voltage, the dislocation defect also reduces the shunt resistance, due to enhanced recombination loss through the defect states. The degree of impact varies significantly among different defects, and the trend is mostly consistent between the spectroscopy signatures (e.g., PL intensity) and optoelectrical characteristics (e.g., I - V characteristics). The defect structure revealed can be used as guidance for the future electronic structure modeling of practically relevant defects. Future efforts will probe devices under high injection current or high illumination density to induce structural modifications of the defects, and investigate the effects.

4. Experimental Section

The GaAs solar cell used in this study consisted of many independent small cells (named as #1, #2, etc.). Each small cell consisted of multiple active regions (labeled as #5-1, #5-2, etc.) that were separated by the top electrode fingers. The details of the device layout are given in the Appendix (see Figure A1 in the Supporting Information). The cell structure contained, from top to bottom, an 80-nm n-type GaAs contact layer doped to $\approx 5 \times 10^{18} \text{ cm}^{-3}$; 50-nm n-type GaInP window layer and 40-nm n-type GaAs emitter layer, both with a doping level $\approx 10^{18} \text{ cm}^{-3}$; 3- μm p-type GaAs absorber layer and 50-nm p-type GaInP back-surface confinement layer, both with a doping level $\approx 7 \times 10^{16} \text{ cm}^{-3}$; 80-nm p-type GaAs buffer layer, then p-type (001) GaAs substrate. Two Au contact electrodes were deposited onto the topmost and bottommost layers. The n-type GaAs contact layer was etched away from the active areas. No antireflection coating was applied. The reflectance at 532 nm was measured to be $R = 0.29$.

Optical and electrical measurements were performed using a modified Horiba LabRam HR 800 Raman microscope. Micro-Raman/PL spectroscopy and mapping were conducted with a 100 \times lens of NA = 0.9, using a 532-nm laser with its power tunable by changing current and/or inserting neutral density filters. The power was measured using a calibrated Thorlabs power meter. EL was powered by a DC power supply, imaged by the video camera of the Raman microscope with a 50 \times long-working distance (LWD) lens with NA = 0.5. The laser-beam-induced current (LBIC) imaging was obtained by scanning the laser focused with the LWD lens. Microscopic I - V characteristics were measured using a Keithley 2401 Source Meter Unit with a focused laser beam. Macroscopic I - V for the device as a whole was measured using a Keithley solar simulator.

GaAs epilayers grown under similar conditions were found to have very low dislocation-type defect densities, on the order of 10^2 cm^{-2} or 1 mm^{-2} .^[5] In the past, low-magnification PL imaging system was typically

used to first identify the approximate location of an individual defect in the GaAs layer of the bare GaAs/GaN double heterostructure, then high-resolution PL mapping was used to determine its accurate location, followed by detailed optical studies.^[5,31] However, the GaAs active or absorber layer in the fabricated device yielded much weaker PL signal due to the minority carrier depletion effect of the p-n junction, which made it difficult to find any significant defect in this device using PL imaging. EL imaging was instead used in this study, since it provided higher sensitivity and efficiency in locating isolated defects that were actually detrimental to the photogenerated and electrically injected carriers. Once a likely defect, typically visible as a dark spot in the EL image, was identified, Raman and PL mappings were carried out near the EL dark spot to confirm that the identified feature was indeed a genuine structural defect of the absorber layer, as opposed to some other irregularity (e.g., processing-induced blemish on the device surface), because the defect of interest has unique spectroscopy features. By analyzing the measured microscopic *I*-*V* curves obtained by separately focusing the 532-nm laser beam at the defect site and away from the site, the impact of the individual defect was able to be directly assessed on the key solar-cell performance parameters, including short circuit current I_{sc} , open circuit voltage V_{oc} , fill factor FF, shunt resistance R_{sh} , and energy conversion efficiency η . After multiple defects on one device were fully characterized, both optically and electrically, and with their locations precisely measured relative to recognizable features nearby, the devices were then examined by TEM.

A FEI Nova 200 NanoLab focused-ion-beam (FIB) system, also equipped with a SEM, was used to prepare cross-section samples with sub-micrometer precision for TEM observation. Specimens were prepared for observation in [110] projection to enable clear identification of any structural defects present in the devices. After thinning to electron transparency at 30 keV, the FIB was further used at 5 keV to remove any remaining amorphized material. For better defect visibility, the specimens were further milled using a Precision Ion Polishing System (PIPS) operated at 1.8 keV, with the sample cooled to liquid-nitrogen temperature to minimize ion-milling artefacts. A Philips CM200-FEG high-resolution TEM, operated at 200 keV, was used for initial imaging. Atomic-resolution images were taken with an aberration-corrected scanning transmission electron microscope (AC-STEM) JEOL ARM200F operated at 200 kV. The beam convergence angle was set at ≈ 22 mrad, while the image collection angles were 0–22 mrad for large-angle bright-field (LABF) imaging and 90–150 mrad for high-angle annular-dark-field (HAADF) imaging.

Supporting Information

Supporting Information is available from the Wiley Online Library or from the author.

Acknowledgements

The work at UNCC was supported by ARO/MURI (W911NF-10-1-0524) and ARO/Electronics (W911NF-16-1-0263). Y.Z. acknowledges the support of Bissell Distinguished Professorship at UNCC. The use of facilities in the John M. Cowley Center for High Resolution Electron Microscopy within the Eyring Materials Center at ASU is greatly acknowledged. The authors thank Prof. Gert Irmer for helpful discussions.

Conflict of Interest

The authors declare no conflict of interest.

Data Availability Statement

The data that supports the findings of this study are available within the article and its supplementary material. Additional data are available from the corresponding authors upon reasonable request.

Keywords

dislocation defects, GaAs solar cells, in operando characterization, *I*-*V* characteristic, photoluminescence, Raman spectroscopy, series mode

Received: August 30, 2020

Revised: November 3, 2020

Published online:

- [1] C. Kittel, *Introduction to Solid State Physics*, John Wiley & Sons, Inc, Hoboken, NJ **2005**.
- [2] M. Lannoo, J. Bourgoin, *Point Defects in Semiconductors I*, Springer-Verlag, Berlin **1981**.
- [3] J. Bourgoin, M. Lannoo, *Point Defects in Semiconductors II*, Springer-Verlag, Berlin **1983**.
- [4] D. B. Holt, B. G. Yacobi, *Extended Defects in Semiconductors: Electronic Properties, Device Effects and Structures*, Cambridge University Press, Cambridge **2007**.
- [5] T. H. Gfroerer, Y. Zhang, M. W. Wanlass, *Appl. Phys. Lett.* **2013**, *102*, 012114.
- [6] F. Zhang, J. F. Castaneda, S. Chen, W. Wu, M. J. DiNezza, M. Lassise, W. Nie, A. Mohite, Y. Liu, S. Liu, D. Friedman, H. Liu, Q. Chen, Y.-H. Zhang, J. Huang, Y. Zhang, *Mater. Today* **2020**, *36*, 18.
- [7] P. Petroff, R. L. Hartman, *Appl. Phys. Lett.* **1973**, *23*, 469.
- [8] C. Kurtziefer, S. Mayer, P. Zarda, H. Weinfurter, *Phys. Rev. Lett.* **2020**, *85*, 290.
- [9] S. Francoeur, J. F. Klem, A. Mascarenhas, *Phys. Rev. Lett.* **2004**, *93*, 067403.
- [10] M. J. Romero, H. Du, G. Teeter, Y. Yan, M. M. Al-Jassim, *Phys. Rev. B* **2011**, *84*, 165324.
- [11] K. Alberi, B. Fluegel, H. Moutinho, R. G. Dhere, J. V. Li, A. Mascarenhas, *Nat. Commun.* **2013**, *4*, 2699.
- [12] H. Liu, Y. Zhang, Y. Chen, P. S. Wijewarnasuriya, *J. Electron. Mater.* **2014**, *43*, 2854.
- [13] B. Fluegel, K. Alberi, M. J. DiNezza, S. Liu, Y. H. Zhang, A. Mascarenhas, *Phys. Rev. Appl.* **2014**, *2*, 034010.
- [14] D. Kuciauskas, T. H. Myers, T. M. Barnes, S. A. Jensen, A. M. A. Motz, *Appl. Phys. Lett.* **2017**, *110*, 083905.
- [15] X. Xu, S. P. Beckman, P. Specht, E. R. Weber, D. C. Chrzan, R. P. Erni, I. Arslan, N. Browning, A. Bleloch, C. Kisielowski, *Phys. Rev. Lett.* **2005**, *95*, 145501.
- [16] D. J. Smith, T. Aoki, J. Mardinly, L. Zhou, M. R. McCartney, *Microscopy* **2013**, *62*, S65.
- [17] C. Li, Y. Wu, T. J. Pennycook, A. R. Lupini, D. N. Leonard, W. Yin, N. Paudel, M. Al-Jassim, Y. Yan, S. J. Pennycook, *Phys. Rev. Lett.* **2013**, *111*, 096403.
- [18] B. Hauer, C. E. Marvinney, M. Lewin, N. A. Mahadik, J. K. Hite, N. Bassim, A. J. Giles, R. E. Stahlbush, J. D. Caldwell, T. Taubner, *Adv. Funct. Mater.* **2020**, *30*, 1907357.
- [19] O. Paetzold, G. Irmer, J. Monecke, S. Griehl, O. Oettel, *J. Raman Spectrosc.* **1993**, *24*, 761.
- [20] P. Martín, J. Jiménez, C. Frigeri, L. F. Sanz, J. L. Weyher, *J. Mater. Res.* **1999**, *14*, 1732.
- [21] Q. Chen, B. S. McKeon, S. Zhang, C.-K. Hu, T. H. Gfroerer, M. W. Wanlass, Y.-H. Zhang, D. J. Smith, Y. Zhang, presented at *IEEE 7th World Conference on Photovoltaic Energy Conversion*, **2018**, p. 3234.
- [22] Q. Chen, Y. Zhang, *Appl. Phys. Lett.* **2013**, *103*, 242104.
- [23] C. Lin, T. A. Merz, D. R. Douth, J. Joh, J. A. d. Alamo, U. K. Mishra, L. J. Brillson, *IEEE Trans. Electron Devices* **2012**, *59*, 2667.
- [24] C. Hu, Q. Chen, F. Chen, T. H. Gfroerer, M. W. Wanlass, Y. Zhang, *Light: Sci. Appl.* **2018**, *7*, 23.
- [25] Z. V. Jibuti, N. D. Dolidze, B. E. Tsekvava, G. L. Eristavi, *Tech. Phys. Lett.* **2003**, *29*, 540.

- [26] A. Mooradian, G. B. Wright, *Phys. Rev. Lett.* **1966**, *16*, 999.
- [27] G. Irmer, M. Wenzel, J. Monecke, *Phys. Rev. B* **1997**, *56*, 9524.
- [28] O. Höhn, A. W. Walker, A. W. Bett, H. Helmers, *Appl. Phys. Lett.* **2016**, *108*, 241104.
- [29] P. Würfel, U. Würfel, *Physics of Solar Cells: From Basic Principles to Advanced Concepts*, Wiley, Hoboken, NJ **2016**.
- [30] M. A. Green, *Silicon Solar Cells*, University of New South Wales, Sydney **1995**.
- [31] F. Chen, Y. Zhang, T. H. Gfroerer, A. N. Finger, M. W. Wanlass, *Sci. Rep.* **2015**, *5*, 10542.
- [32] G. Irmer, M. Jurisch, *Phys. Status Solidi A* **2007**, *204*, 2309.
- [33] H. M. Cheong, A. Mascarenhas, P. Ernst, C. Geng, *Phys. Rev. B* **1997**, *56*, 1882.
- [34] F. Cerdeira, C. J. Buchenauer, F. H. Pollak, M. Cardona, *Phys. Rev. B* **1972**, *5*, 580.
- [35] Y. Arroyo Rojas Dasilva, R. Kozak, R. Erni, M. D. Rossell, *Ultramicroscopy* **2017**, *176*, 11.